1 **Hydrogen-based direct reduction of iron oxide: heterogeneity at**

2 **pellet- and microstructure-scales**

3

4 Yan Ma[1,*], Isnaldi R. Souza Filho[1], Xue Zhang[1,2], Supriya Nandy[1], Pere Barriobero-Vila[3],

5 Guillermo Requena[3,4], Dirk Vogel[1], Michael Rohwerder[1], Dirk Ponge[1], Hauke Springer[1,5],

6 Dierk Raabe[1,*]

7

8 [1] Max-Planck-Institut für Eisenforschung, Max-Planck-Straße 1, 40237 Düsseldorf, Germany

9 [2] Corrosion Center, Institute of Metal Research, Chinese Academy of Sciences, Wencui 62,

10 Shenyang 110016, China

11 [3] Institute of Materials Research, German Aerospace Center (DLR), Linder Höhe, 51147

12 Cologne, Germany

13 [4] Lehr- und Forschungsgebiet Metallische Strukturen und Werkstoffsysteme für die Luft- und

14 Raumfahrt, RWTH Aachen University, 52062 Aachen

15 [5] Institut für Bildsame Formgebung, RWTH Aachen University, Intzestraße 10, 52072 Aachen,

16 Germany

17

18 *Corresponding authors: d.raabe@mpie.de; y.ma@mpie.de

Abstract

Steel production causes a third of all industrial CO_2 emissions due to the use of carbon-based substances as reductants for iron ores, making it a key driver of global warming. Therefore, research efforts aim at replacing these reductants by sustainably produced hydrogen. Hydrogen-based direct reduction (HyDR) is an attractive processing technology, as DR furnaces are routinely operated in the steel industry, yet with CH_4 or CO as reductants. Hydrogen diffuses much faster through shaft furnace pellet agglomerates than carbon-based reductants, but the net reduction kinetics in the HyDR is still too sluggish for high-quantity steel production and the hydrogen consumption exceeds the stoichiometrically required amount substantially. Thus, the present study focuses on a better understanding of the influence of spatial gradients, morphology, and internal microstructures of ore pellets on reduction efficiency and metallization during HyDR. For this purpose, commercial DR pellets were investigated using synchrotron high-energy X-ray diffraction and electron microscopy in conjunction with electron backscatter diffraction as well as chemical probing. Revealing the interplay of the different phases with internal interfaces, free surfaces, and associated nucleation and growth mechanisms provides the basis for developing tailored ore pellets that are better suited for fast and efficient HyDR.

**Keywords:** hydrogen-based direct reduction, iron oxide, microstructure, phase transformation, porosity

1   Introduction

Steel is the dominant metallic alloy system, both in terms of quantity and breadth of applications, serving in transportation, civil and industrial infrastructures, construction, and safety. Steel also enables many clean energy and transport solutions, such as soft magnets in transformers as well as structures and gears in huge wind power plants. Steel can be recycled practically infinitely, by collecting and re-melting its scrap. With an average global recycling

2

rate approaching 70%, it is the most recycled of all materials, more than all other recycled materials combined [1–3]. However, due to steel's role as a backbone material for economic development and its staggering market growth (**Fig. 1** [4,5]), synthesis from steel scrap alone cannot satisfy the global demand [6].
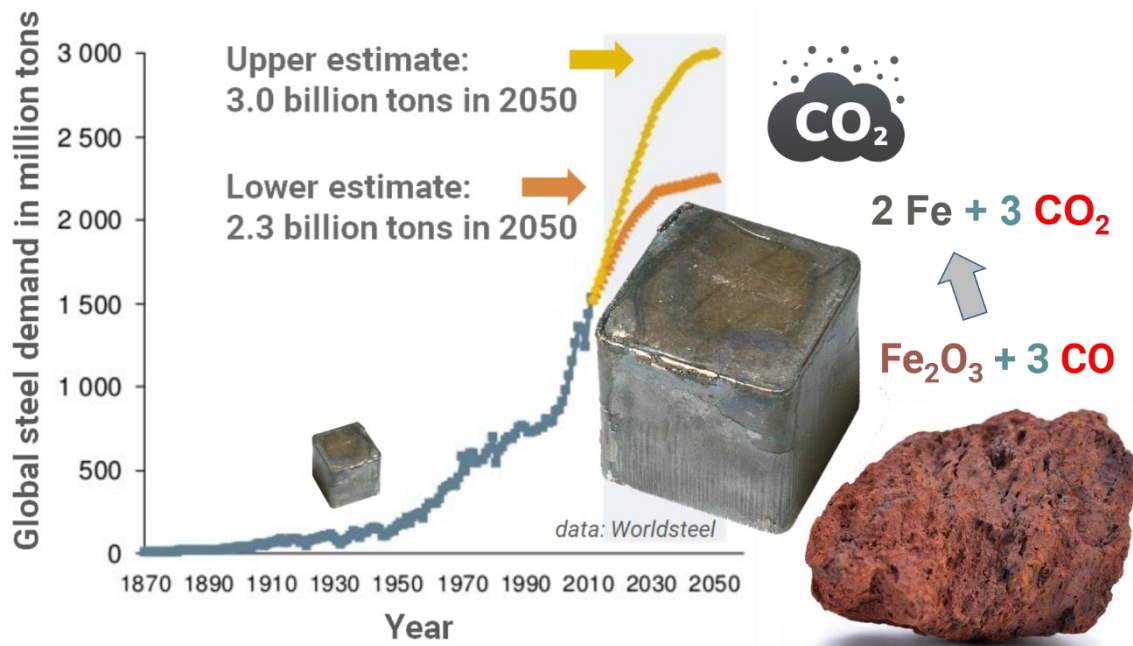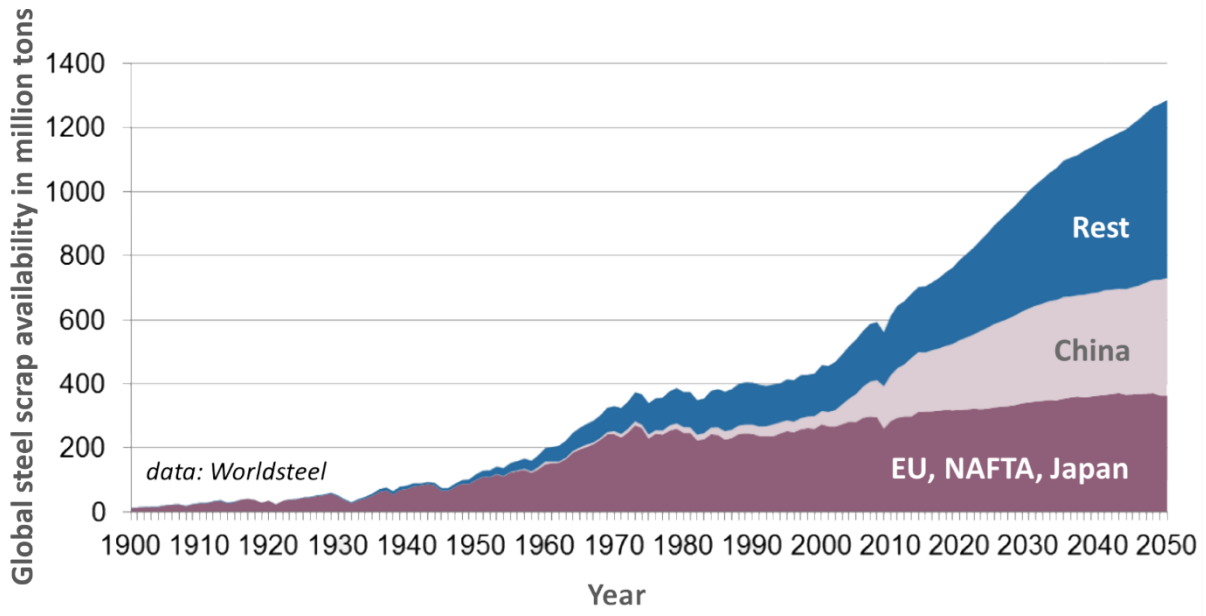

Fig. 1. Development of the global market demand for steel (data taken from Worldsteel Association and from forecast models) [4,5,7]and the carbon-fueled redox reaction that drives the CO₂ emissions from the steel industry.

Also, due to steel's longevity, for instance, in buildings, machines, and vehicles, there is not enough scrap available to meet the current market demands [8]. More than 75% of all steel ever produced is still in use so that globally only about 1/3 of the total steel production can be retrieved from sorting and melting scrap, although the recycled fraction in steelmaking is envisaged to grow, **Fig. 2** [5,6]. An important challenge in using steel scrap also lies in the gradual accumulation of undesired tramp elements such as copper [9–11], which enters

60   particularly through improperly sorted post-consumer scrap and the increasing use of copper in

61   vehicles.

62

Fig. 2. Development of the global steel scrap market (data taken from Worldsteel Association and from [5,6]).

67   Consequently, primary iron synthesis from ore reduction has continued being required in

68   addition to recycling steel scrap for several decades. For these reasons, huge quantities of iron

69   are produced each year by conventional primary production. More than 70% of that global raw

70   iron production stems from blast furnaces, where CO is the major reductant [12]. The current

71   annual consumption of iron ores for this process amounts to the gigantic quantity of about 2.6

72   billion tons, producing about 1.28 billion tons of pig iron, the historical name for the near

73   eutectic iron-carbon alloy tapped from blast furnaces [4]. Each ton of steel produced through

74   the blast furnace (BF) and the subsequent basic oxygen furnace (BOF) route creates about 1.9

75   tons of CO_2 [13]. These numbers qualify iron- and steelmaking as the most staggering single

76   source of greenhouse gas on earth, accounting for about 7-8% of all CO_2 emissions. This

77 number represents 35% of all CO_2 produced in the manufacturing sector [12]. The growth rate

78 projections suggest a massive further increase in these emissions at least up to 2030, if no

79 sustainable and disruptive technology changes are implemented, **Fig. 3** [14–16].

80
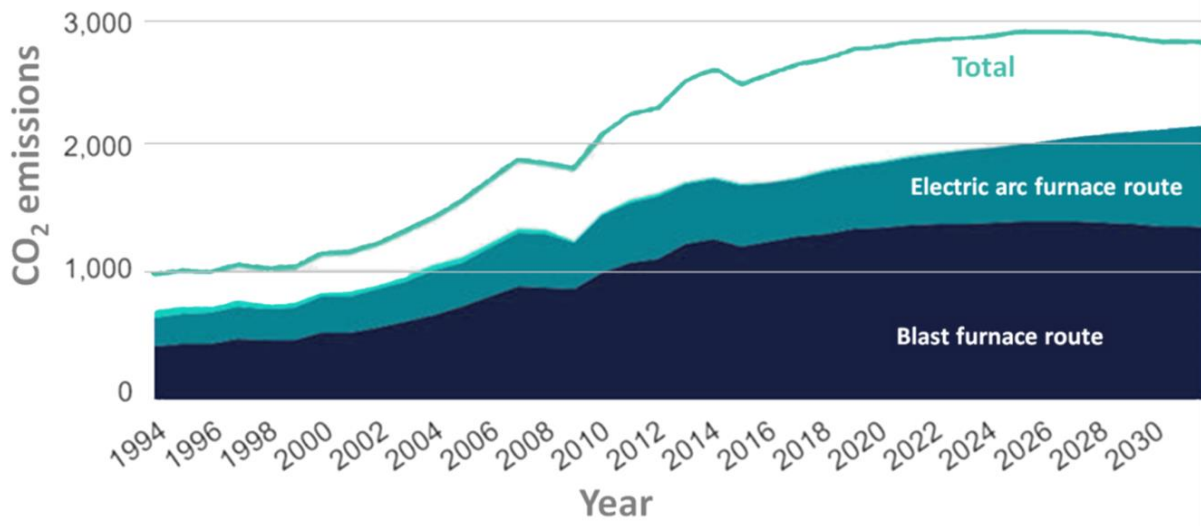
81

82 **Fig. 3. Partially estimated development of the global CO_2 emissions from primary steel production**
83 **(data taken from Worldsteel Association) [4,5,16].**

84

85 Underground CO_2 storage alone, as currently pursued by many steel companies as a transition

86 technology, might cause new environmental burdens for virtually thousands of years. Thus, this

87 cannot be regarded as a responsible long-term solution as gradual CO_2 leakage might harm soil

88 and water [17]. The emission of ~1.9 t CO_2/t steel by the BF-BOF route can be reduced by

89 increasing the amount of scrap. However, it should also be kept in mind that even a 100% scrap-

90 based production through melting in electric arc or induction furnaces still leads to an amount

91 of about 0.3 t CO_2/t steel. This carbon footprint is caused by oxidation and fracture of graphite

92 electrodes as well as by the additional use of fossil fuels in such furnaces. This fossil origin of

93 most electricity is used to heat the furnace and sustain the electric arc. Conventional methane-

94 based direct reduction in conjunction with the subsequent melting of the produced sponge iron

95 in an electric arc furnace results in approximately 0.97 t CO_2/t steel [14]. Fully hydrogen-based

direct reduction (HyDR) followed by the melting of the sponge iron in a conventional electric

arc furnace (operated with graphite electrodes) results in an average <0.1 t CO_2/t steel [18],

when renewable energy is used to produce green hydrogen. It must also be considered that the

production of one ton of steel from 100% scrap or sponge iron by an electric arc furnace process

requires about 9.0 GJ of energy on average. These numbers and facts challenge current

technology standards and operations, against the goals to achieve carbon-lean steel production

and to drastically reduce CO_2 emissions by 80% by 2050, **Fig. 4** [19–24]. In other words, iron-

and steelmaking must be turned from one of the main culprits of global warming to a key

element of a future sustainable and circular economy.
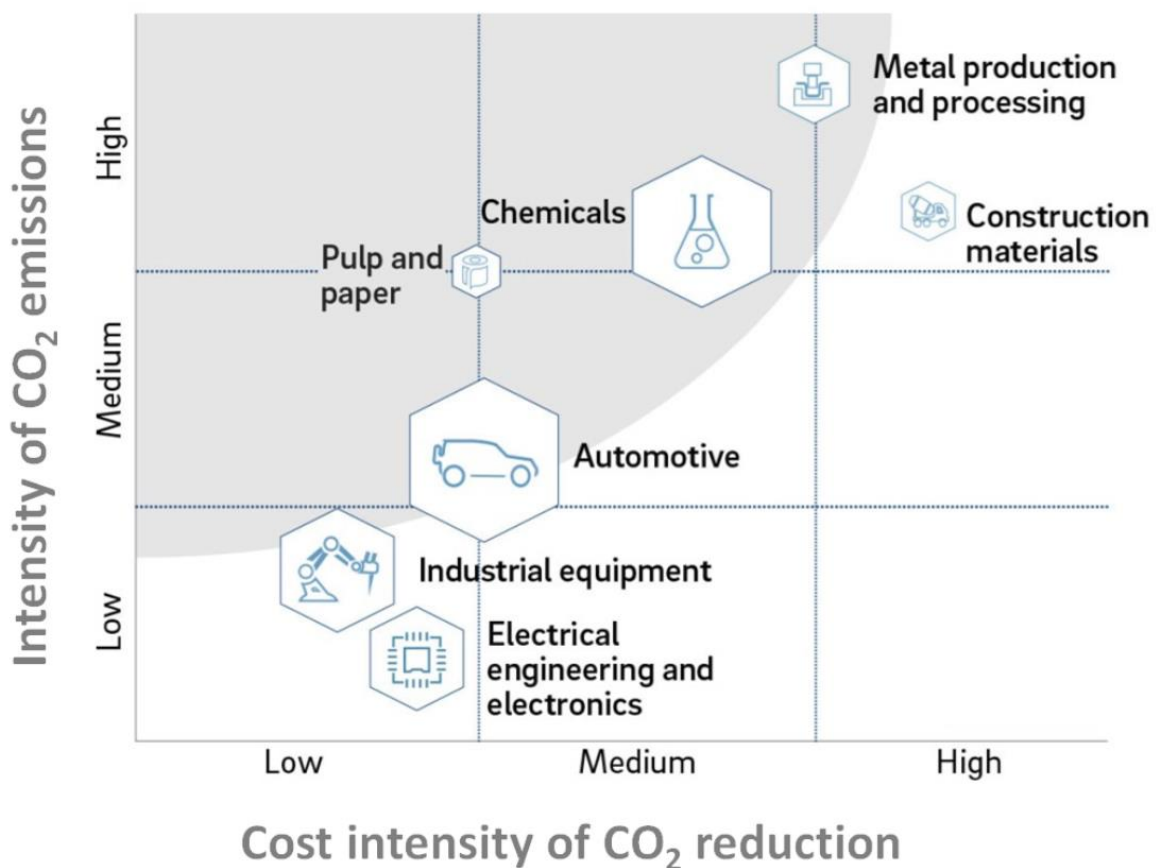
Fig. 4. Analysis of the intensity of the global CO_2 emissions from different industrial sectors versus cost intensity of its reduction. The metal industry is placed in the most challenging upper right corner (data taken from by Roland Berger and Federation of German Industry, BDI) [25].

110

111   Thus, alternative reduction methods potentially with net-zero emissions for extracting iron from

112   its ores have to be urgently studied, identified, matured, and implemented, based on a thorough

113   understanding of the underlying physical and chemical mechanisms. Several strategies are

114   conceivable, including a variety of solid, molecular, ionic, proton, or electron-based reductants

115   and the associated synthesis and reduction methods, in part also combined, **Fig. 5**.

116
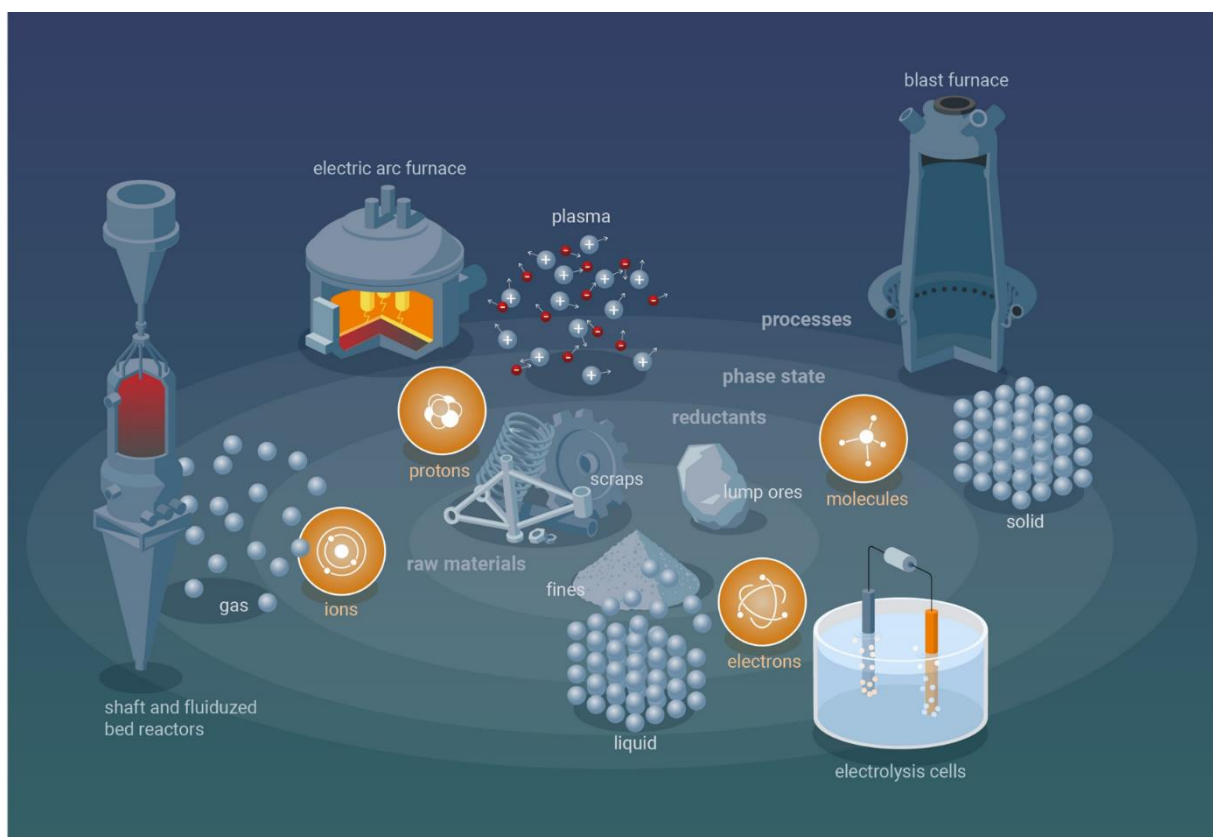
117

118   **Fig. 5. A number of pathways and combinations for melting scrap and reducing iron oxide lump**
119   **ores, pellets, or fines are conceivable, using a wide range of reductants and aggregate states.**

120

121   An alternative approach for large-scale and more sustainable iron oxide reduction is the use of

122   hydrogen gas, its carriers [26], and their plasma variants [27], as reducing agents (instead of

123   carbon), provided they come from sustainable or low-carbon sources [28]. The current study

addresses, particularly, the HyDR with molecular hydrogen, **Fig. 6**. Such solid-state HyDR schemes need to consider three thermodynamic constraints in the design of reactors:

(1) The net energy balance for the complete reduction of iron oxide to iron with molecular hydrogen is endothermic, *i.e.*, it requires external energy to proceed [28], whereas it is exothermic with carbon monoxide.

(2) In the coming transient scenarios for iron ore reduction, green hydrogen is likely not the only reductant (as it is a very expensive feedstock currently), but will likely be mixed with several carbon carriers (*e.g.*, CH_4 and CO) [29,30]. This fact means that the catalytic splitting of the injected molecular dihydrogen into reactive atomic hydrogen ($H_2 \leftrightarrow 2H$) and its reaction with the oxide compete with other reduction reactions [28]. Also, the reaction product, *i.e.*, water, must be removed from the reaction zone as it can re-oxidize or block the reduction front [21]. This negative effect is because water desorbs and diffuses only slowly compared with the atomic reductants. The high partial pressure of water can be detrimental to the nucleation and growth of iron on wüstite (FeO) surfaces [32,33].

(3) The availability of green hydrogen is currently by far too limited to mitigate the steel industry's greenhouse gas output. This discrepancy means that the reduction via grey hydrogen, ammonia, or related hydrogen-carrier substances has to serve as transition technology with a reduced mitigation effect [24,34]. Grey hydrogen, which makes currently more than 95% of the global hydrogen market, comes from steam reforming and partial oxidation of methane, coal gasification, and wet coke gas production. Hydrogen obtained from reforming contains CO as a contaminant, an effect that must be considered in the carbon balance of downstream reactions. A more sustainable transient technology alternative to producing large amounts of hydrogen could be methane pyrolysis, with less harmful solid carbon as a by-product [25].
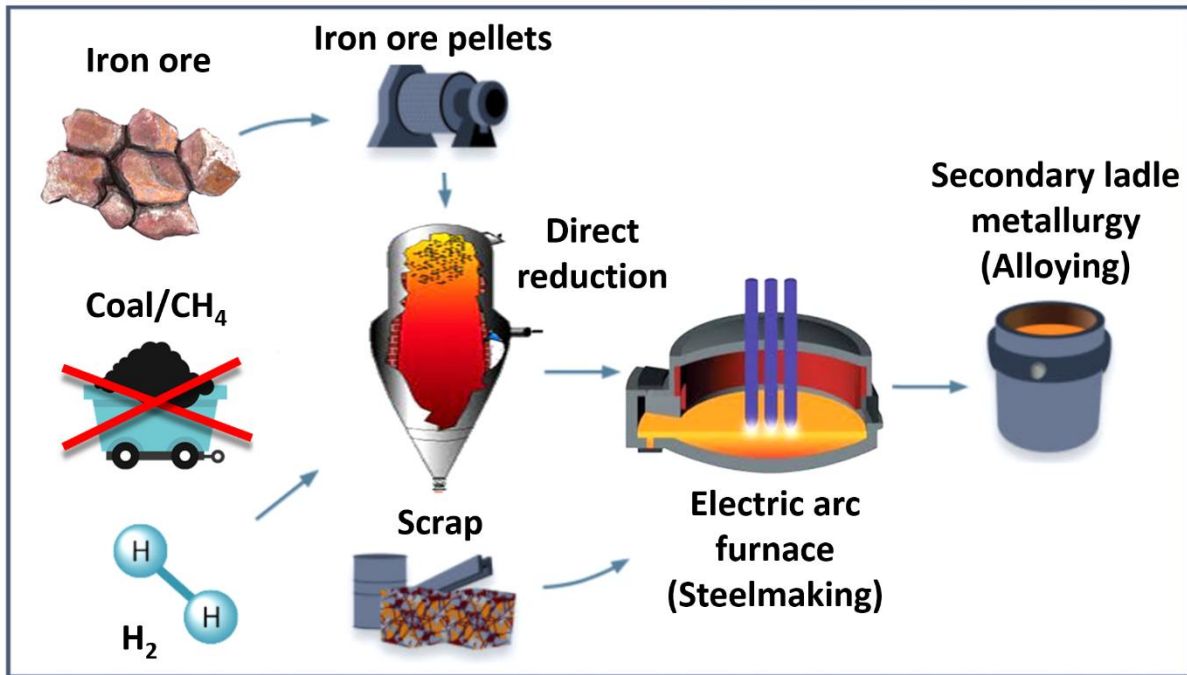
Fig. 6. Two-step process for more sustainable steelmaking: hydrogen-based direct reduction of iron oxide pellets into sponge iron and subsequent melting in an electric arc furnace. The CO_2 balance of hydrogen-based direct reduction depends on electrode materials, heating fuels, methods of hydrogen production, and the (fossil or non-fossil) origin of the electrical power that is being used.

It was observed that hydrogen diffuses faster through the shaft furnace pellet agglomerates than conventional reductant cases, such as CH_4 or CO, which are much larger in molecular size and have thus lower mobilities [35]. Irrespective of this kinetic advantage, the overall reduction kinetics and metallization achieved during the HyDR are not fast enough for the large-volume steel production, which is required to satisfy market demands approaching two billion tons of steel per year, **Fig. 1**. Also, hydrogen supply in these processes exceeds the stoichiometrically required amounts. In this case, additional recycling efforts are currently needed to improve the efficiency of hydrogen usage. Therefore, it is of vital interest to improve the process efficiency, with the pellet macro- and microstructure being of most critical relevance, especially as the pellets available today have been optimized for conventional reduction technology (*i.e.*, blast furnace) or at least for the carbon-based reductants.

The present investigation aims at better understanding the influence of pellet morphology and its internal microstructure on the overall reduction efficiency and metallization[14,26,36,37]. For this purpose, commercial DR pellets have been investigated using synchrotron high-energy X-ray diffraction and electron microscopy in conjunction with electron backscatter diffraction as well as energy-dispersive X-ray spectroscopy. This approach allows revealing the microstructural morphology and spatial gradients of the phase transformations during the HyDR and the interplay of the different phases with the internal interfaces. The obtained results can guide the development of next-generation reactors and pellet feedstock that are better suited for fast and efficient HyDR, to make ironmaking affordably carbon-free.

2 State of the knowledge of direct reduction of solid iron oxide pellets with hydrogen and hydrogen-containing gas mixtures

The direct reduction of solid iron oxide pellets with hydrogen or hydrogen-containing gas mixtures involves multiple phase transformations [28,38–44]. Above 570 °C, it proceeds along the sequence Fe_2O_3 (hematite) $\rightarrow$ Fe_3O_4 (magnetite) $\rightarrow$ $Fe_{(1-X)}O$ (wüstite) $\rightarrow$ α-Fe (BCC iron) or γ-Fe (FCC iron) [24,35,45]. Below 570 °C, wüstite is no longer thermodynamically stable and the reduction reaction proceeds from Fe_2O_3 $\rightarrow$ Fe_3O_4 $\rightarrow$ α-Fe. The overall reaction is endothermic when using H_2 as reductant. Several investigations addressed the use of CO and some also H_2 as a reductants [40,46–48]. These studies focused on the global reduction thermodynamics, kinetics, and the effect of process parameters (*e.g.*, gas flow rate, temperature, and pressure) rather than on the microscopic nucleation and growth mechanisms or on gradients of these features through the feedstock dimensions [40,49–57]. For example, Zieliński *et al*.[49] analyzed the reduction kinetics by exposing hematite to gas mixtures of H_2O and H_2 during temperature-programmed reduction (non-isothermal process). They found that for an H_2O/H_2-

191   ratio above a value of 0.35 the reduction of hematite proceeded in three distinct steps, namely,

192      $Fe_2O_3 \rightarrow Fe_3O_4 \rightarrow FeO \rightarrow Fe$. For H_2O/H_2-ratios below a value of 0.35 two steps were observed:

193      $Fe_2O_3 \rightarrow Fe_3O_4 \rightarrow Fe$. Pineau *et al.* studied the reduction of both, hematite and magnetite

194   [51,52]. The latter is an interesting option as magnetite ores can become a commercially

195   attractive alternative feedstock, when new furnace types and reduction methods enter the

196   market. In addition, their findings indicated that the reaction rate was controlled by the growth

197   of nuclei and phase boundary reactions. Piotrowski *et al.* [58,59] studied the reduction kinetics

198   of hematite to magnetite and to wüstite using thermogravimetry and they described the kinetics

199   by a classical Avrami nucleation and growth model. Patisson *et al.* [14,60] developed more

200   detailed models of the mesoscale structure of the feedstock material, accounting particularly for

201   the role of the granularity of the pellets. Bonalde *et al.* [35] studied the reduction of Fe_2O_3

202   pellets with high inherited porosity exposed to gas mixtures of H_2 and CO. They concluded that

203   the interface reactions and oxygen diffusion acted as competing processes during the first

204   reduction stage, and the internal gas diffusion as a rate-controlling step during the last stage.

205   One assumption of their model was that the phase boundary was moving towards the center of

206   the pellets and that the oxide feedstock material had no porosity or delamination cracks

207   [26,53,61]. However, this assumption does not fully agree with the findings reported in the

208   recent literature [26]. Hence, considering more details about the oxide pellets' defect structures

209   such as interfaces, cracks, pores, and dislocations, *etc.,* prior to reduction (inherited

210   microstructure) and during the reduction (acquired microstructure) and also the dependence of

211   these features on the pellets' mesoscopic heterogeneity and through-pellet spatial gradients is

212   important for understanding the reduction kinetics and metal yield [14,62].

213

214   In the literature, the critical last reduction steps, namely, from wüstite to iron, are discussed in

215   terms of three distinct stages. These are (1) the oxygen-depletion of the oxide, (2) nucleation of

216   iron domains inside of the oxygen-depleted wüstite, and (3) growth of iron crystals [63,64]. The

217   kinetics of the first step [65,66] was reported to depend on the solid-state diffusion of oxygen

218   to the next surface. This depends on the pore and defect structure [14,60]. It was reported that

219   the initially dense wüstite has longer required diffusion lengths for oxygen than a material that

220   contains a high density of pores [26]. Bahgat *et al.* [67–69] studied the role of microstructure

221   in that context. They reported Fe nucleation to occur, particularly, in wüstite and found a high

222   number of iron nuclei particularly near grain boundaries. They interpreted this in terms of faster

223   transport of vacancies and divalent iron cations via interface diffusion [70]. These results clearly

224   showed the role of the microstructure of the pellets in mass transport, nucleation, and growth.

225

226   Also, other groups had revealed the role of the pellet morphology in the reduction kinetics:

227   Hayes [65,71,72], Turkdogan [40,73,74] and Gleitzer [48,75,76] had grouped the

228   morphological changes observed during reduction into the three classes of (a) porous iron, (b)

229   porous wüstite covered by dense iron layers, and (c) dense wüstite covered with dense iron

230   layers. After the nucleation of iron in wüstite, the last reduction stage was often reported to

231   consist of the growth of the iron layers around the wüstite islands [65,72,77]. It was, however,

232   recently found that the freshly formed Fe rarely encloses the inner wüstite completely but

233   undergoes instead frequent Fe/FeO interfacial delamination and cracking phenomena [26]. This

234   observation means that the actual microstructural defect state of the iron layers and the Fe/FeO

235   interfaces forming around the shrinking wüstite regions should be of great importance for the

236   reduction kinetics during this last stage of the reduction [66,73]. In the case that the fresh iron

237   layers form closed core-shell morphologies and are devoid of defects such as interfaces, pores,

238   and cracks, *etc.*, the outbound oxygen diffusion is determined by solid-state diffusion. Hence it

239   is very slow and should be the rate-limiting step of the reaction [78–80].

240

241 However, in case that the iron layer and the Fe/FeO interface undergo fracture and porosity

242 occurs, faster surface-, pipe-, and grain boundary diffusion of oxygen are likely to occur,

243 allowing for much faster transport of oxygen to the nearest internal or external surfaces

244 [35,45,68,81], where it can recombine with adsorbed atomic hydrogen to form water [71]. This

245 fact means that wüstite reduction into iron can be a nucleation-controlled process, particularly

246 during the initial stages, or a more oxygen diffusion-controlled process, particularly during the

247 later stages, depending on the microstructure of the iron that surrounds the wüstite. This kinetic

248 interpretation is plausible as the Fe_2O_3 to Fe_3O_4 reduction as well as the Fe_3O_4 to FeO reduction

249 only stand for modest stoichiometric oxygen losses of 1/9 and 1/4 units of oxygen, respectively,

250 whereas in the final step from FeO to Fe, FeO loses a full unit of oxygen [82–84].

251

252 This discussion suggests that in a mean-field view, the wüstite reduction kinetics has upper and

253 lower bounds, namely, (I) before and (II) after the formation of a dense iron layer on wüstite:

254 Case (I): When H_2 is in direct contact with the oxide, the assumed steps are [85]: (1) H_2

255 molecules diffuse to the surface and (2) react with the oxygen ions from the external surface of

256 the iron oxide, forming water and electrons, part of which reduce Fe^{3+} to Fe^{2+} via the equation

257 $Fe^{3+} + e^- \rightarrow Fe^{2+}$. (3) H_2O moves away from the surface. (4) Fe^{2+} and electrons migrate through

258 the Fe_3O_4 (or FeO) layer to the Fe_2O_3 (or Fe_3O_4) core where they form Fe_3O_4 (or FeO). Combing

259 this picture with the argument of diffusion as the rate-limiting step in the first reduction stages,

260 one hypothesis might be that steps (1) or (3) diffusion of H_2 or H_2O (the latter process should

261 be slower due to the larger molecular size of H_2O) or step (4) (due to inbound migration of Fe^{2+})

262 are the slowest processes.

263 Case (II): After the formation of compact iron, the removal of oxygen from the reaction

264 interface has to take place through that layer. Several rate-determining mechanisms for this

265 have been discussed [49,57,71,83,86–88]. These studies suggest that FeO reduction proceeds

266 in several steps: (i) H_2 gas molecules diffuse to the surface and (ii) react with oxygen at the

267 surface of the iron layer, forming H_2O; (iii) H_2O moves away from the surface; (iv) Due to a

268 gradient in oxygen activity, oxygen diffuses through the iron, leading to (v) iron nucleation and

269 the steady release of oxygen at the reaction front. The net kinetic curves in the literature often

270 do not allow to distinguish whether the rate-determining step is the diffusion corresponding to

271 steps (i) or (iii), or the outbound solid-state diffusion of oxygen taking place in step (iv).

272

273 **3   Experimental set-up and methodology**

274 We investigated the role of the pellet morphology and microstructure in reduction kinetics in

275 the last and most important stage, *i.e.*, from wüstite to iron. Special emphasis was placed on

276 mapping the heterogeneity of the reduction and the radial gradients in reduction kinetics in a

277 partially reduced pellet. For this purpose, we used the same commercial direct-reduction

278 hematite pellets as in a preceding study [26]. The pellet had a diameter of about 11 mm and a

279 chemical composition of 0.36 wt.% FeO, 1.06 wt.% SiO_2, 0.40 wt.% Al_2O_3, 0.73 wt.% CaO,

280 0.57 wt.% MgO, 0.19 wt.% TiO_2, 0.23 wt.% V, 0.10 wt.% Mn, and Fe_2O_3 in balance. The pellet

281 also contained traces of P, S, Na, K, V, and Ti. Details about the pellet's chemistry are provided

282 in [26]. The pellet was isothermally exposed to pure hydrogen with a constant flow rate of

283 30 L/h at 700 °C in a thermogravimetric configuration [89]. The mass loss of the pellet was

284 continuously monitored by the thermal balance during the reduction experiment. The reduction

285 degree was determined from the experimental mass loss divided by the theoretical mass loss,

286 considering hematite being fully reduced into iron.

287

288 The phase distribution along the radius of the partially reduced pellet was characterized by

289 synchrotron high-energy X-ray diffraction (HEXRD). For this purpose, a disk sample with a

290 thickness of ~2 mm was sliced from the center of the spherical pellet using a diamond wire saw.

291   The HEXRD measurements were conducted in transmission mode at the beamline P07 High

292   Energy Materials Science (HEMS) of PETRA III in Deutsches Elektronen-Synchrotron

293   (DESY). The beamline was operated with a fixed beam energy of ~100 keV and the

294   corresponding wavelength of the X-ray beam was 0.124 Å. The probing beam size was 0.5 mm

295    $\times$ 0.5 mm. The Debye-Scherrer diffraction rings were recorded by an area detector PerkinElmer

296   XRD1621 and integrated by the Fit2D software [90]. The phase fraction was calculated based

297   on the Rietveld refinement using the MAUD software [91]. The local microstructure was further

298   analyzed using secondary electron (SE) imaging, electron backscatter diffraction (EBSD), and

299   correlative energy-dispersive X-ray spectroscopy (EDX) in scanning electron microscopy

300   (SEM). The step size for EBSD measurement was 50 nm. The acquired EBSD and EDX data

301   were analyzed using the OIM Analysis$^{\text{TM}}$ V8.6 software package.

302

303   **4   Kinetics of direct reduction of hematite pellet at 700 °C under hydrogen atmosphere**

304   **Fig. 7** presents the experimentally observed reduction kinetics, in terms of the reduction degree

305   for the HyDR of commercial hematite pellets. The data are comparable to those shown in our

306   preceding work [26] and also to the results of other groups [40,49–57]. The reduction rates of

307   the first two reduction steps, *i.e.*, from hematite (Fe_2O_3) to magnetite (Fe_3O_4) and from

308   magnetite further to wüstite ($Fe_{(1-x)}O$), were high, about $0.5\text{-}1.8\times10^{-3}$ s^{-1} (**Fig. 7**b). The wüstite

309   reduction to α-iron (α-Fe) started much slower, at about 0.6×10^{-3} s^{-1} and slowed down rapidly

310   towards the end of the redox reaction. The reduction degree reached 95% after the reduction

311   for about 37 min and 98% after 52 min, indicating that the reduction in this stage was extremely

312   sluggish and complete metallization was not fully obtained. The analysis and discussion of the

313   individual kinetic steps and the roles of some of the underlying microstructure, nucleation,

314   transport, and growth mechanisms have been recently studied by using electron microscopy

315   and atom probe tomography [26] and will thus not be repeated in detail here.

316

317
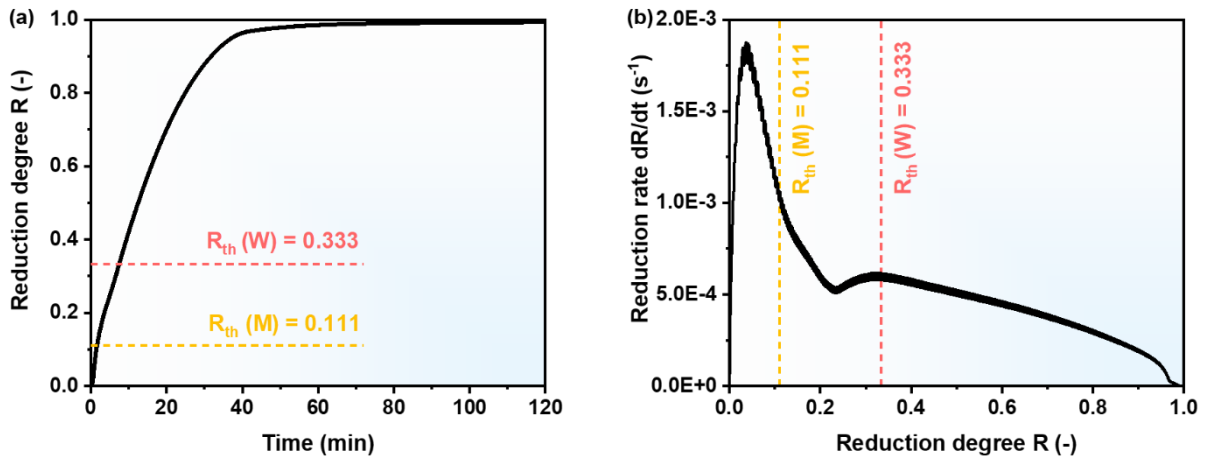
Fig. 7. (a) Reduction degree in terms of mass change as a function of time and (b) reduction rate
(that is the first derivative of the reduction degree) as a function of reduction degree for a
commercial direct-reduction hematite pellet. Reduction in a static bed was conducted under pure
hydrogen gas at a flow rate of 30 L/h at 700 °C. The dotted marker line at a reduction degree of
0.111 indicates the theoretically expected completed reduction from hematite to magnetite and the
line 0.333 the one from magnetite to wüstite. The wüstite reduction proceeds with half an order of
magnitude slower than the preceding reduction steps with a decelerating kinetic trend. The
specimen studied here for radial-gradient effects was taken after an exposure duration of 30
minutes.

327

328   The most characteristic and common feature of all these sequential phase transformation steps

329   during this redox reaction is the gradual deceleration of the transformation rate during the

330   transformation within the same phase regime. An important reason for this was found in the

331   pellet microstructure. During the early stages of the individual phase transformations, the

332   material showed a very rich density of lattice defects, particularly high porosity (due to the

333   gradual mass loss), delamination at the hetero-interfaces, and cracking (due to the high-volume

334   mismatch between the adjacent phases and the resulting mechanical stresses). Another

335   important aspect was that the pellets contain a high-volume fraction of inherited pores. This

336   feature facilitated rapid outbound mass transport (of oxygen) and the removal of water from

337   these surface reaction fronts. Thus, rapid nucleation and growth were always enabled close to

338   these internal free surfaces, particularly at the beginning of the reduction. However, with further

339   progress of the reaction, the remaining oxide regions got increasingly surrounded by the

340   reduction products. As the remaining volume became smaller and highly dispersed, fewer and

341   fewer lattice defects were directly connected to them as pathways for rapid diffusion. In other

342   words, towards the end of these reduction steps, the small remaining oxide regions were less

343   frequently in contact with delamination and cracking features. The remaining oxide regions

344   were surrounded by more and more dense reaction products that impede the removal of oxygen.

345

346   **5   Through-pellet heterogeneity of microstructures during hydrogen-based direct**

347   **reduction at 700 °C**

348   **Fig. 8** presents an overview of the main differences in microstructure, phase composition, and

349   porosity probed by SEM and HEXRD along the radius of a hematite pellet that was reduced

350   with hydrogen at 700 °C after an exposure period of 30 minutes. The results reveal a gradient

351   in microstructure, porosity, and phases between the near-surface and interior regions of the

352   pellet.

353

SEM overview   **SEM images**   **Synchrotron high-energy XRD**

354
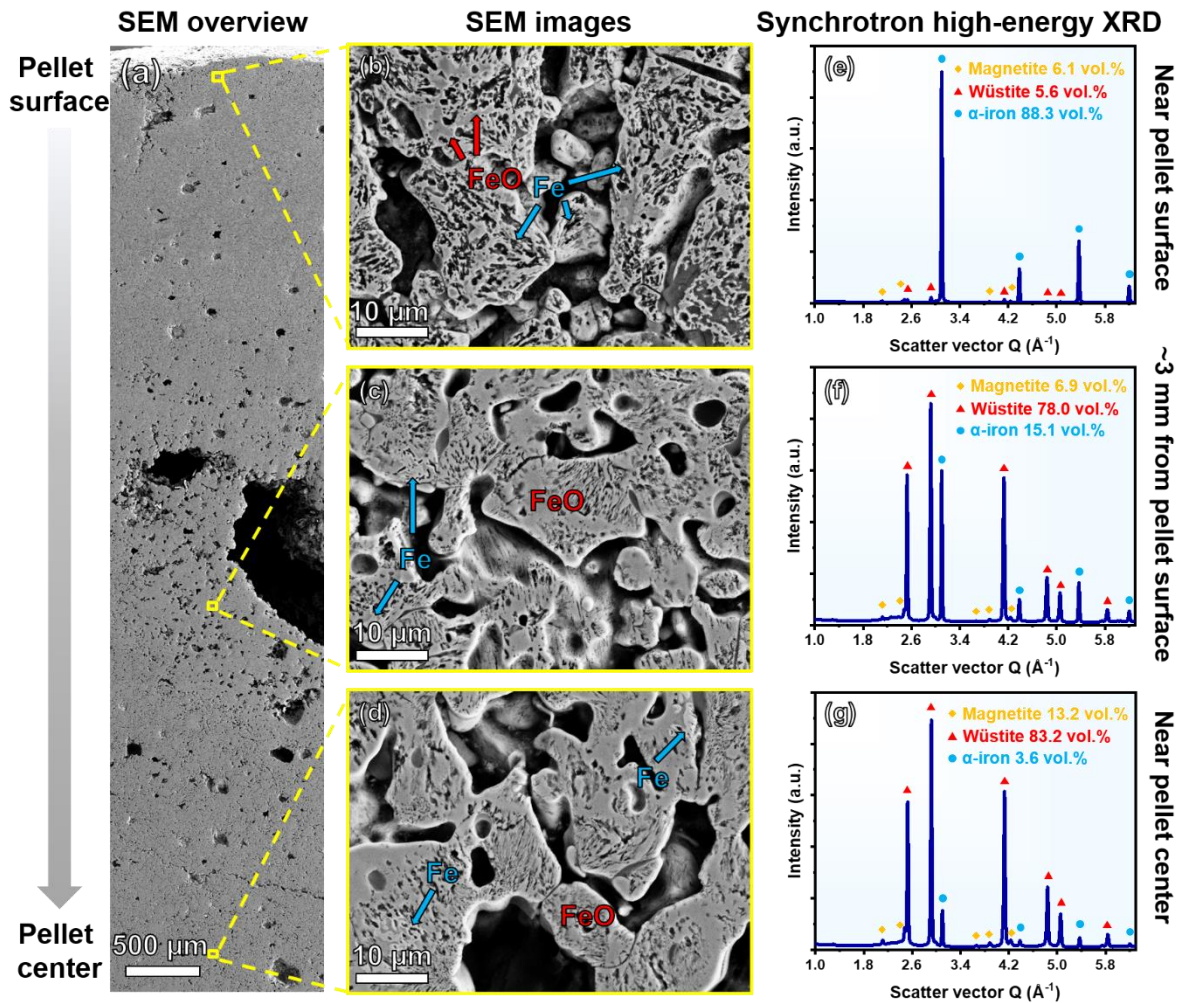
Fig. 8. Overview of the microstructure, phase fractions, and porosity along the radius of a hematite pellet reduced at 700 °C for 30 minutes with pure hydrogen, probed by scanning electron microscopy (SEM) and synchrotron high-energy X-ray diffraction (HEXRD). (a) SEM overview of the pellet structure between the surface and center regions. Magnified SEM images of the microstructures in (b) the near-surface region, (c) the region ~3 mm below the surface, and (d) the center region of the pellet. (e) – (f) Bulk HEXRD analysis of the spatial distribution of phase constituents along the pellet radius (probing volume of 0.5 mm × 0.5 mm × 2 mm).

The pellets are granular agglomerates consisting of sintered polycrystalline substructure units that are hierarchically stacked together with large pore regions among them (*e.g.*, the visible pores in **Fig. 8**a and the large pores among the sintered substructure units in **Fig. 8**b-d). These general aspects of the pellet morphology, its granular substructure, and their role on reduction kinetics were studied in detail in the papers of Patisson *et al.* [14,36,92] and Kim *et al.* [26]. In the near-surface regions of the pellets, oxygen can rapidly diffuse outbound either towards the

outer free surface of the pellet or towards the adjacent free volume in the form of the pores that were inherited from the pelletizing process. On these free surfaces, the oxygen can combine with hydrogen to form water.

Another kinetically relevant factor is that hydrogen intrudes from the outer free pellet surfaces so that the outer regions are naturally the ones getting reduced most rapidly. This basic kinetic picture is supported by the microstructure gradient along the pellet radius measured by the HEXRD (**Fig.** 8). The surface area of the pellet revealed the highest metallization degree of 88.3 vol.% α-iron, with remaining small fractions of wüstite 5.6 vol.% and magnetite 6.1 vol.%. Conversely, the metallization dropped down to 15.1 vol.% α-iron in the region about 3 mm below the pellet surface, with a large portion of remaining iron oxides, *i.e.*, 78.0 vol.% wüstite and 6.9 vol.% magnetite. There was no significant difference in the phase fractions in the center region of the pellet (83.2 vol.% wüstite, 13.2 vol.% magnetite, and 3.6 vol.% α-iron) compared with the region about 3 mm below the pellet surface. This HEXRD result indicated a very drastic difference in the reduction rate between the near-surface regions of the pellet and its interiors.

6   Local microstructure

Fehler! Verweisquelle konnte nicht gefunden werden. shows the microstructure and phase topology in a region about 2 mm below the surface of the partially reduced pellet. The reduced iron is visible in these backscattered electron images due to its bright contrast, while the wüstite appears in a darker grey contrast. The black regions are the pores that were inherited from pellet sintering and also formed due to the mass loss during the reduction process. The important microstructure features at this last reduction stage (*i.e.*, from wüstite to iron) will be discussed in this section.

19

394
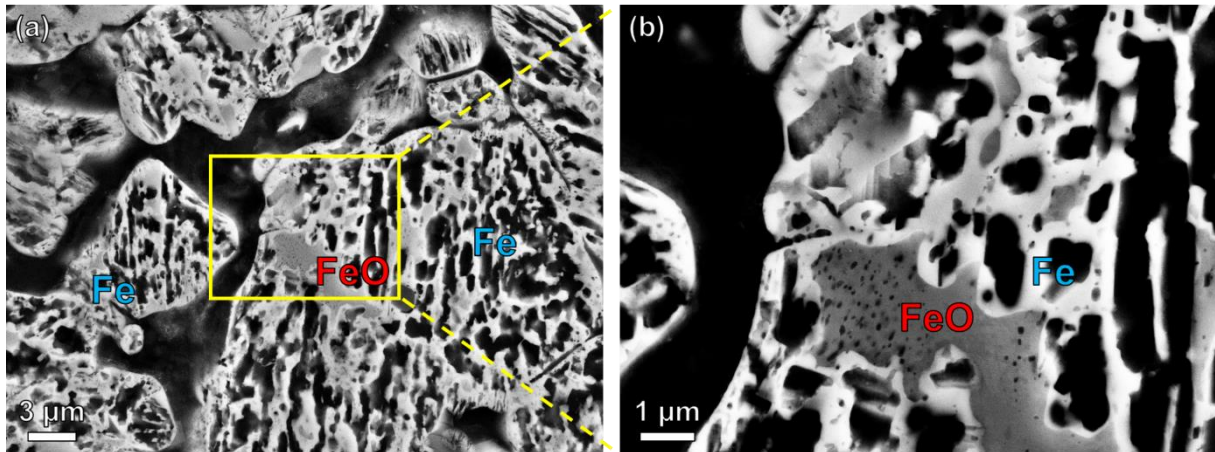
Fig. 9. Backscatter electron (BSE) images taken at higher magnification, revealing the local distribution of pores, wüstite, and iron in the region about 2 mm below the pellet surface after reduction at 700 °C for 30 minutes with pure hydrogen.

These micrographs shown in **Fig. 9** reveal several fundamental features that seem to be characteristic for the entire HyDR process when using such pellets. One important feature is that all the iron has formed adjacent to the free surfaces. This feature matches the kinetic expectations regarding the fast hydrogen intrusion due to gaseous surface diffusion along these free volume regions, as well as the fast removal rate of oxygen at these internal interfaces, where water was formed and stored. At the beginning of reduction, the hydrogen ingress and the oxygen removal as well as recombination into water occurred only at the large percolating pore regions inherited from pelletizing process. However, it must be considered that some of these pores evolved during the gradual removal of the oxygen during the reduction. This phenomenon can be clearly seen in terms of the evolving nanoscale porosity inside of the wüstite region (**Fig. 9b**). With the ongoing gradual removal of oxygen, these pores will further grow and locally recombine into larger ones over the course of the reduction.

413 It is also likely that the nucleation barrier for the formation of iron is smaller at the free surface

414 than in the interior. This is due to (a) the heterogeneous nucleation advantage where some of

415 the required interface energy is already provided by these inner open surfaces and (b) the

416 relaxation of the elastic stresses upon iron nucleation at the surface. Owing to the large volume

417 difference between the iron and the wüstite of more than 40% [93], the latter aspect is assumed

418 to have a substantial energetic influence on the nucleation barrier. When considering the

419 associated elastic misfit stresses in the calculation of the required nucleation energies (which

420 would be expected in the gigapascal range, if no plastic relaxation occurs), the surface

421 nucleation barriers for forming iron are much lower than those in the interior.

422

423 Another important microstructure feature is that some of the remaining inner wüstite regions

424 became increasingly encapsulated by iron. Only a few delamination features and pores were

425 observed at the hetero-interfaces (**Fehler! Verweisquelle konnte nicht gefunden werden.**).

426 This behavior was also revealed by the composition and phase maps shown in **Fig. 10**. The

427 consequence of this composite phase topology is that the outbound oxygen transport must

428 proceed through the surrounding bulk iron regions. This makes the last reduction stages

429 relatively slow and the reduction rate continuously drop, **Fig. 7** [26]. Such a microscopic core-

430 shell behavior is different from the reduction behavior in the early stage of the wüstite to iron

431 transition, where many delamination features were observed at the wüstite/iron hetero-

432 interfaces [26].
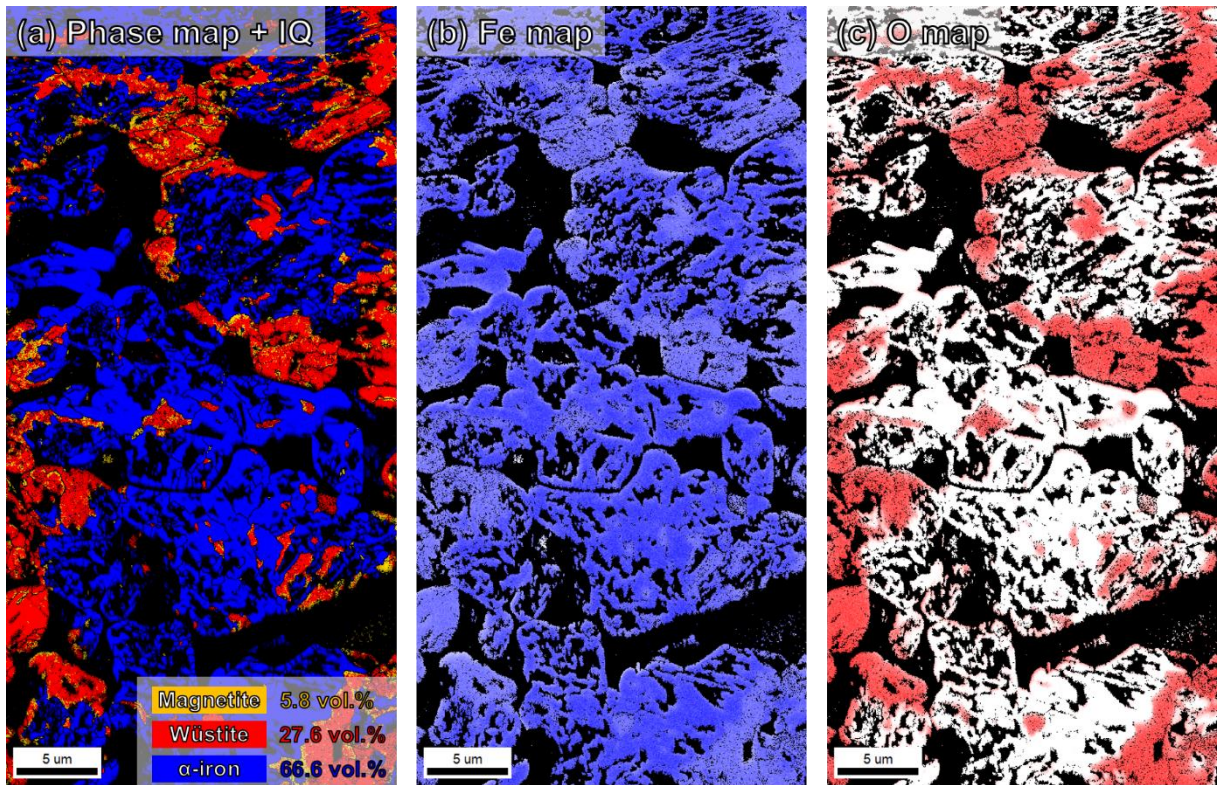
Fig. 10. Local phase and elemental distribution in the region about 2 mm below the surface of the partially reduced pellet probed by electron backscatter diffraction (EBSD) and energy-dispersive X-ray spectroscopy (EDX). (a) EBSD phase map imposed on image quality (IQ); (b) EDX iron distribution map; and (c) EDX oxygen distribution map.

7 Discussion of the role of the through-pellet heterogeneity in hydrogen-based direct reduction kinetics and metallization

The results reveal a large difference in reduction rate and metallization along the pellet radius. This observation raises concerns not only regarding the overall sluggish reduction rate due to these gradient effects but also regarding the low efficiency in the use of hydrogen. The decarbonization of the global steel industry with the aid of techniques such as the HyDR makes only sense when green hydrogen is used. This aspect means that the beneficial total efficiency and life-cycle assessment regarding the carbon footprint require hydrogen produced by sustainable energy sources, which is a very expensive product. Thus, hydrogen should be used in such reduction processes as efficiently as possible. In other words, a total efficiency

22

449 assessment of the HyDR processes requires to not only consider the total energy balance but

450 also the total efficiency in hydrogen consumption as an essential cost and sustainability factor.

451

452 The large through-pellet gradient of reduction kinetics observed in this study suggests

453 reconsidering the suitability of the current commercial pellet design for the HyDR processes.

454 Particularly, considering the unique physical properties of molecular hydrogen, *i.e.*, its smaller

455 molecular size and lower viscosity compared with CO or CH_4, the gas transport phenomena in

456 the HyDR could be very different from the processes with carbon-based reductants. Thus,

457 further studies will be placed to assess the effect of pellet size, porosity, and microstructure on

458 the gaseous percolation both experimentally and theoretically. In this case, better

459 characterization of the porous structures is highly needed, especially revealing the three-

460 dimensional connectivity of the pores. This information is of importance for disentangling the

461 percolation paths. With the further help of the fluid dynamics simulation, the underlying gas

462 transport phenomena can be better understood. The gained knowledge will allow for the

463 knowledge-based pellet design, which enables accelerating the overall reduction kinetics in the

464 HyDR processes.

465

466 **8   Conclusions**

467 In this study, we investigated the spatial gradient of the microstructure of a partially reduced

468 commercial hematite pellet and its influence on reduction kinetics during the hydrogen-based

469 direct reduction. The microstructure analysis along the pellet radius revealed strong

470 heterogeneity of the reduction rate. The surface region of the pellet showed a high metallization

471 of 88 vol.% α-iron, whereas in the center region of the pellet there was only about 4 vol.% α-

472 iron. The local microstructure analysis further suggested that the outbound diffusion of oxygen

473 was substantially delayed not only in the center areas of the pellets but also in the sub-surface

zones as the remaining wüstite islands were encapsulated by iron. Also, it seems that even the observed abundance of defect-mediated transport pathways for fast oxygen diffusion is insufficient to warrant more homogeneous and rapid reduction kinetics. The results, therefore, suggest that the current commercial pellet design is not suited for efficient hydrogen-based direct reduction. The current findings could assist in guiding the optimization of pellets, in terms of size, strength, composition, porosity, and microstructure, to meet the demands of fast and efficient hydrogen-based direct reduction.

Acknowledgements

References

[1]   M. Ashby, Materials and the Environment: Eco-informed Material Choice: Second Edition, 2012. https://doi.org/10.1016/C2010-0-66554-0.

[2]   A.C.H. Allwood, J. M. Cullen, J. M. Carruth, M. A. Cooper, D.R. McBrien, M. Milford, R.L. Moynihan, M.C. Patel, S. Bauer, Sustainable materials: With both eyes open, UIT Cambridge Ltd, Cambridge, England, 2012. https://doi.org/10.1016/s1369-7021(12)70169-4.

499   [3]   T.E. Graedel, J. Allwood, J.P. Birat, M. Buchert, C. Hagelüken, B.K. Reck, S.F. Sibley,

500   G. Sonnemann, What do we know about metal recycling rates?, J. Ind. Ecol. 15 (2011)

501   355–366. https://doi.org/10.1111/j.1530-9290.2011.00342.x.

502   [4]   E. Basson, Major steel-producing countries 2018 and 2019 million, 2020 World Steel

503   Fig. (2020) 1–8. http://www.worldsteel.org/wsif.php.

504   [5]   C. The World Steel Association, Brussels, Belgium; Beijing, Worldsteel Statistics, Steel

505   Mark.   Steel   Stat.   Pages.   (2021).   https://www.worldsteel.org/steel-by-

506   topic/statistics/World-Steel-in-Figures.html.

507   [6]   J. Oda, K. Akimoto, T. Tomoda, Long-term global availability of steel scrap, Resour.

508   Conserv. Recycl. 81 (2013) 81–91. https://doi.org/10.1016/j.resconrec.2013.10.002.

509   [7]   J. Morfeldt, W. Nijs, S. Silveira, The impact of climate targets on future steel production

510   - An analysis based on a global energy system model, J. Clean. Prod. 103 (2015) 469–

511   482. https://doi.org/10.1016/j.jclepro.2014.04.045.

512   [8]   H. Ohno, K. Matsubae, K. Nakajima, Y. Kondo, S. Nakamura, T. Nagasaka, Toward the

513   efficient recycling of alloying elements from end of life vehicle steel scrap, Resour.

514   Conserv. Recycl. 100 (2015) 11–20. https://doi.org/10.1016/j.resconrec.2015.04.001.

515   [9]   K.E. Daehn, A. Cabrera Serrenho, J.M. Allwood, How Will Copper Contamination

516   Constrain Future Global Steel Recycling?, Environ. Sci. Technol. 51 (2017) 6599–6606.

517   https://doi.org/10.1021/acs.est.7b00997.

518   [10]   M. Haupt, C. Vadenbo, C. Zeltner, S. Hellweg, Influence of Input-Scrap Quality on the

519   Environmental Impact of Secondary Steel Production, J. Ind. Ecol. 21 (2017) 391–401.

520   https://doi.org/10.1111/jiec.12439.

521   [11]   K.E. Daehn, A.C. Serrenho, J. Allwood, Finding the Most Efficient Way to Remove

522   Residual Copper from Steel Scrap, Metall. Mater. Trans. B Process Metall. Mater.

523   Process. Sci. 50 (2019) 1225–1240. https://doi.org/10.1007/s11663-019-01537-9.

524   [12]   D. Raabe, C.C. Tasan, E.A. Olivetti, Strategies for improving the sustainability of

525 structural metals, Nature. 575 (2019) 64–74. https://doi.org/10.1038/s41586-019-1702-

526 5.

527 [13] M. Flores-Granobles, M. Saeys, Minimizing CO2emissions with renewable energy: A

528   comparative study of emerging technologies in the steel industry, Energy Environ. Sci.

529   13 (2020) 1923–1932. https://doi.org/10.1039/d0ee00787k.

530 [14] F. Patisson, O. Mirgaux, Hydrogen ironmaking: How it works, Metals (Basel). 10 (2020)

531   1–15. https://doi.org/10.3390/met10070922.

532 [15] P. Enkvist, P. A. Klevnas, The Circular Economy - A Powerful Force for Climate

533   Mitigation, 2018.

534 [16] W. Jaimes, S. Maroufi, Sustainability in steelmaking, Curr. Opin. Green Sustain. Chem.

535   24 (2020) 42–47. https://doi.org/10.1016/j.cogsc.2020.01.002.

536 [17] M. Celia, S. Bachu, Geological Sequestration of CO2Is Leakage Unavoidable and

537   Acceptable?, in: Greenh. Gas Control Technol. - 6th Int. Conf., 2003: pp. 477–482.

538   https://doi.org/10.1016/b978-008044276-1/50076-3.

539 [18] V. Vogl, M. Åhman, L.J. Nilsson, Assessment of hydrogen direct reduction for fossil-

540   free   steelmaking,   J.   Clean.   Prod.   203   (2018)   736–745.

541   https://doi.org/10.1016/j.jclepro.2018.08.279.

542 [19] S. Lechtenböhmer, C. Schneider, M.Y. Roche, S. Höller, Re-industrialisation and low-

543   carbon economy-can they go together? Results from stakeholder-based scenarios for

544   energy-intensive industries in the German state of North Rhine Westphalia, Energies. 8

545   (2015) 11404–11429. https://doi.org/10.3390/en81011404.

546 [20] E. de Pee, Arnout; Pinner, Dickon; Occo, Roelofsen; Somers, Ken; Witteveen, Maaike;

547   Speelman, Decarbonization of industrial sectors: the next frontier, McKinsey Co. (2018)

548   68. https://www.mckinsey.com/~/media/McKinsey/Business Functions/Sustainability

549   and Resource Productivity/Our Insights/How industry can move toward a low carbon

550   future/Decarbonization-of-industrial-sectors-The-next-frontier.ashx.

551 [21] F. Hanrot, J.P. Birat, G. Danloy, Perspectives of CO2 emissions reduction in iron & steel

552   european industries, in: 2nd Int. Meet. Ironmak. 1st Int. Symp. Iron Ore Parallel Event-

553   5th Japan-Brazil Symp. Dust Process. Metall. Ind., 2004.

554 [22] N.A. Warner, Towards Zero CO2 Continuous Steelmaking Directly from Ore, Metall.

555   Mater. Trans. B Process Metall. Mater. Process. Sci. 45 (2014) 2080–2096.

556   https://doi.org/10.1007/s11663-014-0136-6.

557 [23] K. Nishioka, Y. Ujisawa, S. Tonomura, N. Ishiwata, P. Sikstrom, Sustainable Aspects of

558   CO2 Ultimate Reduction in the Steelmaking Process (COURSE50 Project), Part 1:

559   Hydrogen Reduction in the Blast Furnace, J. Sustain. Metall. 2 (2016) 200–208.

560   https://doi.org/10.1007/s40831-016-0061-9.

561 [24] M. Fischedick, J. Marzinkowski, P. Winzer, M. Weigel, Techno-economic evaluation of

562   innovative steel production technologies, J. Clean. Prod. 84 (2014) 563–580.

563   https://doi.org/10.1016/j.jclepro.2014.05.063.

564 [25] B. Langefeld, Climate protection in the manufacturing sector: Challenges and solutions,

565   (2021). https://www.rolandberger.com/en/Insights/Publications/Climate-protection-in-

566   the-manufacturing-sector-Challenges-and-solutions.html.

567 [26] S.H. Kim, X. Zhang, Y. Ma, I.R. Souza Filho, K. Schweinar, K. Angenendt, D. Vogel,

568   L.T. Stephenson, A.A. El-Zoka, J.R. Mianroodi, M. Rohwerder, B. Gault, D. Raabe,

569   Influence of microstructure and atomic-scale chemistry on the direct reduction of iron

570   ore with hydrogen at 700°C, Acta Mater. 212 (2021) 116933.

571   https://doi.org/10.1016/j.actamat.2021.116933.

572 [27] I.R. Souza Filho, Y. Ma, M. Kulse, D. Ponge, B. Gault, H. Springer, D. Raabe,

573   Sustainable steel through hydrogen plasma reduction of iron ore: Process, kinetics,

574   microstructure, chemistry, Acta Mater. 213 (2021) 116971.

575   https://doi.org/10.1016/j.actamat.2021.116971.

576 [28] D. Spreitzer, J. Schenk, Reduction of Iron Oxides with Hydrogen—A Review, Steel Res.

Int. 90 (2019) 1900108. https://doi.org/10.1002/srin.201900108.

[29] K. Nishihiro, T. Maeda, K. ichiro Ohno, K. Kunitomo, Effect of H2 concentration on carbon deposition reaction by CO–H2 gas mixture at 773 K to 973 K, ISIJ Int. 59 (2019) 634–642. https://doi.org/10.2355/isijinternational.ISIJINT-2018-393.

[30] K. Nishihiro, T. Maeda, K. ichiro Ohno, K. Kunitomo, Effect of temperature and CO2 concentration on gasification behavior of carbon fiber containing fine iron particles, ISIJ Int. 59 (2019) 2142–2148. https://doi.org/10.2355/isijinternational.ISIJINT-2019-240.

[31] A. Sormann, J. Schenk, M.N. Seftejani, M.A. Zarl, D. Spreitzer, Hydrogen - The Way to a Carbon free Steelmaking, in: ADMET Conf. Lviv, Ukr., 2018.

[32] H. Nogami, Y. Kashiwaya, D. Yamada, Simulation of blast furnace operation with intensive hydrogen injection, ISIJ Int. 52 (2012) 1523–1527. https://doi.org/10.2355/isijinternational.52.1523.

[33] A.J. Fortini, D.D. Perlmutter, Porosity effects in hydrogen reduction of iron oxides, AIChE J. 35 (1989) 1245–1252. https://doi.org/10.1002/aic.690350803.

[34] M. Weigel, M. Fischedick, J. Marzinkowski, P. Winzer, Multicriteria analysis of primary steelmaking technologies, J. Clean. Prod. 112 (2016) 1064–1076. https://doi.org/10.1016/j.jclepro.2015.07.132.

[35] A. Bonalde, A. Henriquez, M. Manrique, Kinetic analysis of the iron oxide reduction using hydrogen-carbon monoxide mixtures as reducing agent, ISIJ Int. 45 (2005) 1255–1260. https://doi.org/10.2355/isijinternational.45.1255.

[36] A. Ranzani Da Costa, D. Wagner, F. Patisson, Modelling a new, low CO2 emissions, hydrogen steelmaking process, J. Clean. Prod. 46 (2013) 27–35. https://doi.org/10.1016/j.jclepro.2012.07.045.

[37] C.E. Seaton, J.S. Foster, J. Velasco, Reduction Kinetics of Hematite and Magnetite Pellets Containing Coal Char., Trans. Iron Steel Inst. Japan. 23 (1983) 490–496. https://doi.org/10.2355/isijinternational1966.23.490.

603   [38]   A.A. El-Geassy, K.A. Shehata, S.Y. Ezz, Mechanism of iron oxide reduction with

604   hydrogen/carbon monoxide mixtures, Trans Iron Steel Inst Jpn. 17 (1977) 629–635.

605   [39]   D. Guo, M. Hu, C. Pu, B. Xiao, Z. Hu, S. Liu, X. Wang, X. Zhu, Kinetics and

606   mechanisms of direct reduction of iron ore-biomass composite pellets with hydrogen gas,

607   Int.   J.   Hydrogen   Energy.   40   (2015)   4733–4740.

608   https://doi.org/10.1016/j.ijhydene.2015.02.065.

609   [40]   E.T. Turkdogan, J. V. Vinters, Gaseous reduction of iron oxides: Part I. Reduction of

610   hematite   in   hydrogen,   Metall.   Mater.   Trans.   B.   2   (1971)   3175–3188.

611   https://doi.org/10.1007/bf02814970.

612   [41]   J.F. Plaul, W. Krieger, E. Bäck, Reduction of fine ores in argon-hydrogen plasma, Steel

613   Res. Int. 76 (2005) 548–554. https://doi.org/10.1002/srin.200506055.

614   [42]   K. Badr, E. Back, W. Krieger, Plasma reduction of iron oxide by methane gas and its

615   process   up-scaling,   Steel   Res.   Int.   78   (2007)   275–280.

616   https://doi.org/10.1002/srin.200705892.

617   [43]   H. Purwanto, H.M. Salleh, A.N. Rozhan, A.S. Mohamad, A. Zakiyuddin, Phase change

618   of iron ore reduction process using EFB as reducing agent at 900-1200°C, in: IOP Conf.

619   Ser. Mater. Sci. Eng., 2018. https://doi.org/10.1088/1757-899X/342/1/012054.

620   [44]   Z. Chen, J. Dang, X. Hu, H. Yan, Reduction kinetics of hematite powder in hydrogen

621   atmosphere   at   moderate   temperatures,   Metals   (Basel).   8   (2018).

622   https://doi.org/10.3390/met8100751.

623   [45]   N.G. Gallegos, M.A. Apecetche, Kinetic study of haematite reduction by hydrogen, J.

624   Mater. Sci. 23 (1988) 451–458. https://doi.org/10.1007/BF01174669.

625   [46]   M.V.C. Sastri, R.P. Viswanath, B. Viswanathan, Studies on the reduction of iron oxide

626   with   hydrogen,   Int.   J.   Hydrogen   Energy.   7   (1982)   951–955.

627   https://doi.org/10.1016/0360-3199(82)90163-X.

628   [47]   H.Y. Lin, Y.W. Chen, C. Li, The mechanism of reduction of iron oxide by hydrogen,

629   Thermochim. Acta. 400 (2003) 61–67. https://doi.org/10.1016/S0040-6031(02)00478-1.

630   [48]   M. Moukassi, P. Steinmetz, B. Dupre, C. Gleitzer, A study of the mechanism of reduction

631   with hydrogen of pure wustite single crystals, Metall. Trans. B. 14 (1983) 125–132.

632   https://doi.org/10.1007/BF02670879.

633   [49]   J. Zieliński, I. Zglinicka, L. Znak, Z. Kaszkur, Reduction of Fe2O3 with hydrogen, Appl.

634   Catal. A Gen. 381 (2010) 191–196. https://doi.org/10.1016/j.apcata.2010.04.003.

635   [50]   M.J. Tiernan, P.A. Barnes, G.M.B. Parkes, Reduction of iron oxide catalysts: The

636   investigation of kinetic parameters using rate perturbation and linear heating

637   thermoanalytical   techniques,   J.   Phys.   Chem.   B.   105   (2001)   220–228.

638   https://doi.org/10.1021/jp003189+.

639   [51]   A. Pineau, N. Kanari, I. Gaballah, Kinetics of reduction of iron oxides by H2. Part I: Low

640   temperature   reduction   of   hematite,   Thermochim.   Acta.   447   (2006)   89–100.

641   https://doi.org/10.1016/j.tca.2005.10.004.

642   [52]   A. Pineau, N. Kanari, I. Gaballah, Kinetics of reduction of iron oxides by H2. Part II.

643   Low temperature reduction of magnetite, Thermochim. Acta. 456 (2007) 75–88.

644   https://doi.org/10.1016/j.tca.2007.01.014.

645   [53]   R. Walker, D. Carpenter, Influence of reducing gas composition on the structure and

646   reducibitlity of iron oxides, J Iron Steel Inst. 208 (1970) 67.

647   [54]   H. Kister, U. Pueckoff, H.J. Engell, Einfluß von Wasserstoffzusätzen zu

648   Kohlenmonoxidhaltigen Gas-Gemischen auf die Reduktion von Wüstit, Arch

649   Eisenhuettenwes. 43 (1972) 737–745.

650   [55]   H. Zuo, C. Wang, J. Dong, K. Jiao, R. Xu, Reduction kinetics of iron oxide pellets with

651   H2   and   CO   mixtures,   Int.   J.   Miner.   Metall.   Mater.   22   (2015)   688–696.

652   https://doi.org/10.1007/s12613-015-1123-x.

653   [56]   Q.T. Tsay, W.H. Ray, J. Szekely, The modeling of hematite reduction with hydrogen

654   plus carbon monoxide mixtures: Part I. The behavior of single pellets, AIChE J. 22

(1976) 1064–1072. https://doi.org/10.1002/aic.690220617.

[57]   E. Kawasaki, J. Sanscrainte, T.J. Walsh, Kinetics of reduction of iron oxide with carbon monoxide and hydrogen, AIChE J. 8 (1962) 48–52. https://doi.org/10.1002/aic.690080114.

[58]   K. Piotrowski, K. Mondal, H. Lorethova, L. Stonawski, T. Szymański, T. Wiltowski, Effect of gas composition on the kinetics of iron oxide reduction in a hydrogen production process, Int. J. Hydrogen Energy. 30 (2005) 1543–1554. https://doi.org/10.1016/j.ijhydene.2004.10.013.

[59]   K. Piotrowski, K. Mondal, T. Wiltowski, P. Dydo, G. Rizeg, Topochemical approach of kinetics of the reduction of hematite to wüstite, Chem. Eng. J. 131 (2007) 73–82. https://doi.org/10.1016/j.cej.2006.12.024.

[60]   H. Hamadeh, O. Mirgaux, F. Patisson, Detailed modeling of the direct reduction of iron ore in a shaft furnace, Materials (Basel). 11 (2018). https://doi.org/10.3390/ma11101865.

[61]   J. Sarkar, T.R.G. Kutty, D.S. Wilkinson, J.D. Embury, D.J. Lloyd, Tensile properties and bendability of T4 treated AA6111 aluminum alloys, Mater. Sci. Eng. A. 369 (2004) 258–266. https://doi.org/10.1016/j.msea.2003.11.022.

[62]   S.Y. Luo, Y.M. Zhou, C.J. Yi, X. Yue, Z.G. Li, Ironmaking by direct reduction of iron ore-biomass composite pellets using biomass syngas, Beijing Keji Daxue Xuebao/Journal Univ. Sci. Technol. Beijing. 35 (2013) 856–861.

[63]   J.R. Gavarri, C. Carel, The complex nonstoichiometry of wüstite Fe1-zO: Review and comments, Prog. Solid State Chem. 53 (2019) 27–49. https://doi.org/10.1016/j.progsolidstchem.2018.10.001.

[64]   J. Berthon, A. Revcolevschi, H. Morikawa, B. Touzelin, Growth of wustite (Fe1-x O) crystals of various stoichiometries, J. Cryst. Growth. 47 (1979) 736–738. https://doi.org/10.1016/0022-0248(79)90020-4.

[65]   D.H.S. John, P.C. Hayes, Microstructural features produced by the reduction of wustite

in H2/H2O gas mixtures, Metall. Trans. B. 13 (1982) 117–124. https://doi.org/10.1007/BF02666962.

[66] D.H.S. John, S.P. Matthew, P.C. Hayes, The breakdown of dense iron layers on wustite in CO/CO2 and H2/H2O systems, Metall. Trans. B. 15 (1984) 701–708. https://doi.org/10.1007/BF02657292.

[67] M. Bahgat, Y. Sasaki, S. Hijino, M. Iguchi, K. Ishii, The effect of grain boundaries on iron nucleation during wüstite reduction process, ISIJ Int. 44 (2004) 2023–2028. https://doi.org/10.2355/isijinternational.44.2023.

[68] M. Bahgat, M.H. Khedr, Reduction kinetics, magnetic behavior and morphological changes during reduction of magnetite single crystal, Mater. Sci. Eng. B Solid-State Mater. Adv. Technol. 138 (2007) 251–258. https://doi.org/10.1016/j.mseb.2007.01.029.

[69] Y. Sasaki, M. Bahgat, M. Iguchi, K. Ishii, The preferable growth direction of iron nuclei on wüstite surface during reduction, ISIJ Int. 45 (2005) 1077–1083. https://doi.org/10.2355/isijinternational.45.1077.

[70] S. El Moujahid, A. Rist, The nucleation of iron on dense wustite: A morphological study, Metall. Trans. B. 19 (1988) 787–802. https://doi.org/10.1007/BF02650198.

[71] M. Farren, S.P. Matthew, P.C. Hayes, Reduction of solid wustite in H2/H2O/CO/CO2 gas mixtures, Metall. Trans. B. 21 (1990) 135–139. https://doi.org/10.1007/BF02658125.

[72] D.H.S. John, S.P. Matthew, P.C. Hayes, Establishment of product morphology during the initial stages of wustite reduction, Metall. Trans. B. 15 (1984) 709–717. https://doi.org/10.1007/BF02657293.

[73] E.T. Turkdogan, R.G. Olsson, J. V. Vinters, Gaseous reduction of iron oxides: Part II. Pore characteristics of iron reduced from hematite in hydrogen, Metall. Mater. Trans. B. 2 (1971) 3189–3196. https://doi.org/10.1007/bf02814971.

[74] E.T. Turkdogan, J. V. Vinters, Gaseous reduction of iron oxides: part III., Met. Trans. 3

707   (1972) 1561–1574. https://doi.org/10.1007/BF02643047.

708   [75]   M. Ettabirou, B. Dupré, C. Gleitzer, Nucleation and early growth of magnetite on

709   synthetic and natural hematite crystals, React. Solids. 1 (1986) 329–343.

710   https://doi.org/10.1016/0168-7336(86)80025-0.

711   [76]   F. Adam, B. Dupre, C. Gleitzer, Cracking of hematite crystals during their low-

712   temperature reduction into magnetite, Solid State Ionics. 32–33 (1989) 330–333.

713   https://doi.org/10.1016/0167-2738(89)90237-3.

714   [77]   S. Geva, M. Farren, D.H.S. John, P.C. Hayes, The effects of impurity elements on the

715   reduction of wustite and magnetite to iron in CO/CO2 and H2/H2O gas mixtures, Metall.

716   Trans. B. 21 (1990) 743–751. https://doi.org/10.1007/BF02654253.

717   [78]   J. Takada, M. Adachi, Determination of diffusion coefficient of oxygen in α-iron from

718   internal oxidation measurements in Fe-Si alloys, J. Mater. Sci. 21 (1986) 2133–2137.

719   https://doi.org/10.1007/BF00547959.

720   [79]   R. Barlow, P.J. Grundy, The determination of the diffusion constants of oxygen in nickel

721   and α-iron by an internal oxidation method, J. Mater. Sci. 4 (1969) 797–801.

722   https://doi.org/10.1007/BF00551075.

723   [80]   H. Hagi, Diffusion Coefficient of Hydrogen in Iron without Trapping by Dislocations

724   and   Impurities,   Mater.   Trans.   JIM.   35   (1994)   112–117.

725   https://doi.org/10.2320/matertrans1989.35.112.

726   [81]   A.A. El-Geassy, F.O. El-Kashif, M.I. Imasr, A.A. Omar, Kinetics and Mechanisms of

727   Re-oxiation of Freshly Reduced Iron Compacts, ISIJ Int. 34 (1994) 541–547.

728   https://doi.org/10.2355/isijinternational.34.541.

729   [82]   P. Pourghahramani, E. Forssberg, Reduction kinetics of mechanically activated hematite

730   concentrate with hydrogen gas using nonisothermal methods, Thermochim. Acta. 454

731   (2007) 69–77. https://doi.org/10.1016/j.tca.2006.12.023.

732   [83]   A.A. Barde, J.F. Klausner, R. Mei, Solid state reaction kinetics of iron oxide reduction

using hydrogen as a reducing agent, in: Int. J. Hydrogen Energy, Elsevier Ltd, 2016: pp. 10103–10119. https://doi.org/10.1016/j.ijhydene.2015.12.129.

[84] G.S. Parkinson, Iron oxide surfaces, Surf. Sci. Rep. 71 (2016) 272–365. https://doi.org/10.1016/j.surfrep.2016.02.001.

[85] C. Feilmayr, A. Thurnhofer, F. Winter, H. Mali, J. Schenk, Reduction behavior of hematite to magnetite under fluidized bed conditions, ISIJ Int. 44 (2004) 1125–1133. https://doi.org/10.2355/isijinternational.44.1125.

[86] Y.D. Wang, X.N. Hua, C.C. Zhao, T.T. Fu, W. Li, W. Wang, Step-wise reduction kinetics of Fe2O3 by CO/CO2 mixtures for chemical looping hydrogen generation, Int. J. Hydrogen Energy. 42 (2017) 5667–5675. https://doi.org/10.1016/j.ijhydene.2017.01.159.

[87] S.K. El-Rahaiby, Y.K. Rao, The kinetics of reduction of iron oxides at moderate temperatures, Metall. Trans. B. 10 (1979) 257–269. https://doi.org/10.1007/BF02652470.

[88] S. Hayashi, Y. Iguchi, Morphology of iron reduced from wustite with h2-h2o-h2s mixtures, ISIJ Int. 29 (1989) 596–604. https://doi.org/10.2355/isijinternational.29.596.

[89] M. Auinger, D. Vogel, A. Vogel, M. Spiegel, M. Rohwerder, A novel laboratory set-up for investigating surface and interface reactions during short term annealing cycles at high temperatures, Rev. Sci. Instrum. 84 (2013). https://doi.org/10.1063/1.4817310.

[90] A.P. Hammersley, FIT2D: A multi-purpose data reduction, analysis and visualization program, J. Appl. Crystallogr. 49 (2016) 646–652. https://doi.org/10.1107/S1600576716000455.

[91] L. Lutterotti, Total pattern fitting for the combined size-strain-stress-texture determination in thin film diffraction, Nucl. Instruments Methods Phys. Res. Sect. B Beam Interact. with Mater. Atoms. 268 (2010) 334–340. https://doi.org/10.1016/j.nimb.2009.09.053.

759   [92]   D. Wagner, O. Devisme, F. Patisson, D. Ablitzer, A laboratory study of the reduction of

760   iron oxides by hydrogen, in: 2006 TMS Fall Extr. Process. Div. Sohn Int. Symp., 2006:

761   pp. 111–120.

762   [93]   W. Mao, W.G. Sloof, Reduction Kinetics of Wüstite Scale on Pure Iron and Steel Sheets

763   in Ar and H2 Gas Mixture, Metall. Mater. Trans. B Process Metall. Mater. Process. Sci.

764   48 (2017) 2707–2716. https://doi.org/10.1007/s11663-017-1037-2.

765